

# Femtosecond transparency in the extreme ultraviolet

Michal Tarana\* and Chris H. Greene

*Department of Physics and JILA, University of Colorado,*

*Boulder, Colorado 80309-0440, USA*

## Abstract

Electromagnetically induced transparency-like behavior in the extreme ultraviolet (XUV) is studied theoretically, including the effect of intense 800 nm laser dressing of He  $2s2p$  ( $^1P^o$ ) ( $^1P^o$ ) and  $2p^2$  ( $^1S^e$ ) ( $^1S^e$ ) autoionizing states. We present an *ab initio* solution of the time-dependent Schrödinger equation (TDSE) in an *LS*-coupling configuration interaction basis set. The method enables a rigorous treatment of optical field ionization of these coupled autoionizing states into the  $N = 2$  continuum in addition to  $N = 1$ . Our calculated transient absorption spectra show encouraging agreement with experiment.

---

\* michal.tarana@jila.colorado.edu

## 5 I. INTRODUCTION

6 The use of two laser fields to dress the eigenstates of a three-level system has attracted  
7 significant attention over past two decades [1]. The interaction of light with a coherent  
8 atomic ensemble leads to important quantum interference phenomena, including electro-  
9 magnetically induced transparency (EIT) [2, 3], in which the laser-induced coherence of  
10 atomic states leads to quantum interference between the excitation pathways that control  
11 the optical response. It can be used to manipulate the linear and nonlinear susceptibilities  
12 of matter from the near-infrared to ultraviolet. This has resulted in applications such as  
13 slowed and stored light as well as nonlinear frequency conversion [4].

14 Presently there is great interest in the application of light in the X-ray regime, produced  
15 by high-order harmonics and free electron lasers, to investigate novel coherent X-ray optical  
16 phenomena. In this context, ultrafast electron dynamics of the autoionization processes  
17 in atoms has gained attention in recent years. The advent of femtosecond and attosecond  
18 XUV laser pulses in a pump-probe setting has made it possible to follow these processes  
19 in real time [5]. These experiments involving two coherent laser pulses allow study of the  
20 time-resolved interaction of the direct ionization pathway with pathways involving one or  
21 more resonant states. This opens the possibility of new ways to monitor and control the au-  
22 toionization dynamics [6, 7] and consequently the XUV absorption properties of the dressed  
23 medium.

24 Theoretical studies due to Bachau *et al.* [8] and Themelis *et al.* [9] predicted the transfor-  
25 mation of the original unperturbed Fano line-shape [10] into an Autler-Townes doublet due  
26 to Rabi flopping between a pair of coherently-coupled doubly-excited states. Loh *et al.* [11]  
27 observed EIT-like behavior in an XUV probe induced by coherent coupling of the  $2s2p$  ( $^1P^o$ )  
28 and  $2p^2$  ( $^1S^e$ ) doubly-excited states in helium, where the XUV probe was created from IR  
29 laser-produced high-order harmonics. Specifically, that study used a femtosecond infrared  
30 (IR) pulse both to couple the doubly-excited states and to produce the probe pulse. Both  
31 *et al.* [12] predicted an EIT for X-rays in laser dressed neon. More recently, Ranitovic *et al.*  
32 [13] used a two-color multiphoton ionization of helium in combined IR laser and XUV high  
33 harmonic fields to control the transparency. They showed that this scheme can induce full  
34 electromagnetic transparency.

35 Quantum mechanical calculations of the photoabsorption spectra for the dressed atoms

36 represent a challenge for theory, especially when the dressing laser pulse couples doubly-  
37 excited states. The time-consuming solution of the time-dependent Schrödinger equation  
38 (TDSE) is required for every photon energy of the probe pulse. An alternative theoretical  
39 treatment has been introduced by Tong and Toshima [14] and successfully used in Ref. [13].  
40 It is based on the Floquet representation and on the calculation of the autocorrelation  
41 function that is independent of the probe laser photon energy. Therefore, the time and  
42 memory demanding numerical calculation of the autocorrelation function is performed only  
43 once. Since the photoabsorption cross section has a simple analytical dependence on the  
44 autocorrelation function, its calculation is not difficult. However, the approach introduced in  
45 Ref. [14] involves a diagonalization of the Hamiltonian matrix in the Floquet representation,  
46 typically having dimensions  $10^6 \times 10^6$  and this step is still challenging for a supercomputer.

47 To our knowledge, there is no method which enables a routine theoretical calculation of  
48 the photoabsorption spectra in the presence of a strong dressing laser pulse. The aim of the  
49 present work is to make a step towards the improvement of the theoretical treatment of this  
50 problem. This study deals with the modified Fano line-shape in the photoabsorption spec-  
51 trum of the He 2s2p ( $^1P^o$ ) doubly-excited state caused by the coupling of this state with the  
52  $2p^2$  ( $^1S^e$ ) doubly-excited state by an IR femtosecond pulse. Loh *et al.* [11] studied this effect  
53 experimentally and interpreted obtained results as EIT-like behavior. A simplified three-  
54 level[15] model treatment of this problem was included in Ref. [11]. The model describes  
55 formation of an Autler-Townes doublet and takes into account the effect of the optical field  
56 ionization of the doubly-excited states due to the IR dressing laser using a somehow *ad hoc*  
57 adaptation of the Ammosov-Delone-Krainov (ADK) method. Our approach presented in  
58 this work is based on the numerical solution of the TDSE. It takes into account the pos-  
59 sible coupling of more than two autoionizing states and the continuum in principle more  
60 accurately than the approach presented in Ref. [11]. Therefore, the present treatment of  
61 the optical field ionization of the doubly-excited states due to the coupling laser field is more  
62 quantitative as well. Photoabsorption spectra calculated using parameters corresponding to  
63 the experimental setup used in Ref. [11] are compared with results obtained for reduced IR  
64 pulse intensity and for significantly reduced IR detuning. Comparison of all these results  
65 allows us to study the effect of the optical field ionization and of the IR laser detuning on  
66 the formation of EIT-like structures in the spectra.

67 The rest of this paper is organized as follows: The theoretical approach and assumptions

68 of our model are discussed in Sec. II. A detailed description of the field free Hamiltonian  
69 and static photoabsorption spectrum is given in Sec. III, while Sec. IV discusses the pho-  
70 toabsorption yields of the dressed atom.

71 Atomic units are used throughout the rest of the paper.

## 72 II. THEORETICAL APPROACH

73 The model introduced in the present study is based on the experimental publication of to  
74 Loh *et al.* [11]. In that experiment the  $2s2p$  ( $^1P^o$ ) ( $^1P^o$ ) and  $2p^2$  ( $^1S^e$ ) ( $^1S^e$ ) doubly-excited  
75 states of He are coupled by a strong 800 nm field. The  $2s2p$  ( $^1P^o$ ) and  $2p^2$  ( $^1S^e$ ) states  
76 are located at 60.15 [16] and 62.06 eV [17] above the  $1s^2$  ground state, respectively. This  
77 system is then probed after a variable time delay by an XUV pulse. The XUV probe pulse  
78 is produced with a table-top, laser-based setup by high-order harmonic generation (HHG).  
79 The authors use a commercial Ti:sapphire laser system (2.4 W, 800 nm, 42 fs, 1 kHz) to  
80 produce the optical dressing and HHG beam. The estimated photon flux at the source is  $10^5$   
81 photons per pulse for the high-order harmonic centered at 60.2 eV. The XUV pulse duration  
82 is estimated to be 30 fs FWHM. The dressing pulse peak intensity is  $1.4 \times 10^{13}$  W/cm<sup>2</sup>  
83 and its duration is 42 fs FWHM. The spectrometer used in [11] measures the transmission  
84 spectrum instead of the absorption spectrum. The unknown fraction of dressed atoms in the  
85 interaction volume prevents the photoabsorption spectrum of the dressed atom from being  
86 retrieved experimentally. Therefore, authors measure the transient absorption spectra and  
87 identify EIT-like structures.

88 The XUV laser pulse couples the  $1s^2$  ground state with the  $2s2p$  ( $^1P^o$ ) autoionizing state  
89 with energy 35.56 eV above the  $N = 1$  ionization threshold. Therefore, it is reasonable  
90 to assume that every absorption of an XUV photon leads to photoionization. The aim of  
91 the present work is to calculate the population of the ground state at the end of the pulse  
92 as a function of the XUV photon energy  $\hbar\omega_X$  for different dressing-probe time delays  $t_D$ .  
93 The computed loss of the ground state population is interpreted as the total photoabsorp-  
94 tion yield. Its comparison with the yields obtained when the IR pulse is absent allows for  
95 recognition of EIT-like structures.

96 Helium is a two-electron system. The two-particle basis set used in the present calcula-  
97 tions consists of  $LS$ -coupled independent-particle basis functions [18, 19]. The Hamiltonian

98 for the interaction of each electron with the core is

$$h(\mathbf{r}) = -\frac{1}{2}\nabla^2 - \frac{2}{r}, \quad (1)$$

99 where  $\mathbf{r}$  is the coordinate of the electron with respect to the nucleus. The corresponding (ra-  
100 dially rescaled) single-particle radial wave function  $\varphi(r)$  for an electron with orbital angular  
101 momentum  $l$ , is given by

$$\left(-\frac{1}{2}\frac{d^2}{dr^2} + \frac{l(l+1)}{2r^2} - \frac{2}{r}\right)\varphi(r) = \varepsilon\varphi(r). \quad (2)$$

102 The atomic Hamiltonian including the interaction between the electrons is

$$H = h(\mathbf{r}_1) + h(\mathbf{r}_2) + \frac{1}{r_{12}}, \quad (3)$$

103 where  $r_{12} = |\mathbf{r}_1 - \mathbf{r}_2|$  is the distance between the electrons.

104 To calculate the time development of the ground state population we solve the TDSE for  
105 the two linearly-polarized laser fields in the length gauge:

$$i\frac{\partial}{\partial t}\Psi(\mathbf{r}_1, \mathbf{r}_2, t) = [H + D_I(t + t_D) + D_X(t) + V_C]\Psi(\mathbf{r}_1, \mathbf{r}_2, t), \quad (4)$$

106 where  $D_{I,X}(t) = \mathbf{E}_{I,X}(t) \cdot \mathbf{d} = \mathbf{E}_{I,X}(t) \cdot (\mathbf{r}_1 + \mathbf{r}_2)$  are the interaction operators for the IR  
107 and XUV laser pulse in the dipole approximation, respectively.  $V_C$  denotes the complex  
108 absorbing potential (CAP) added to treat ionization properly within the context of a finite  
109 volume calculation. As in the experimental convention, a positive time delay  $t_D$  means that  
110 the XUV probe pulse center arrives later than the pump pulse center. The electric fields  
111  $\mathbf{E}_I(t)$  and  $\mathbf{E}_X(t)$  are given by

$$\mathbf{E}_{I,X}(t) = \hat{\mathbf{z}}E_{I,X}(t) = \hat{\mathbf{z}}E_{I,X}^0 f(t) \cos(\omega_{I,X}t), \quad (5)$$

112 where  $\omega_{I,X}$  are the IR and XUV laser field frequencies,  $\hat{\mathbf{z}}$  is the unit vector along the po-  
113 larization axis,  $E_{I,X}^0$  are the peak amplitudes of the electric fields and  $f_{I,X}(t)$  are the pulse  
114 envelopes. Throughout this work it is assumed that both envelopes have the  $\cos^2$  form

$$f_I(t) = \begin{cases} \cos^2(\pi t/\tau_I), & -\tau_I/2 \leq t \leq \tau_I/2 \\ \sqrt{0.13} \cos^2(\pi(t - t_P)/\tau_{IP}), & -\tau_{IP}/2 \leq t - t_P \leq \tau_{IP}/2 \\ 0, & \text{otherwise,} \end{cases} \quad (6)$$

115 resp.,

$$f_X(t) = \begin{cases} \cos^2(\pi t/\tau_X), & -\tau_X/2 \leq t \leq \tau_X/2 \\ 0, & \text{otherwise,} \end{cases} \quad (7)$$

116 where  $\tau_{I,X}$  denote the durations of the respective laser pulses. The second term in Eq. (6)  
 117 denotes the IR postpulse which appears in the experiment [11] with time delay  $t_P = 88$  fs  
 118 and duration  $\tau_{IP} = 30$  fs. The CAP used in the present calculations has the form [20]

$$V_C = \begin{cases} 0, & r_1 \leq r_b \text{ and } r_2 \leq r_b \\ -i\eta [(r_1 - r_b)^2 + (r_2 - r_b)^2], & \text{otherwise,} \end{cases} \quad (8)$$

119 where  $\eta > 0$  is the strength of the CAP and  $r_b$  is the inner boundary of the absorber. The  
 120 TDSE (4) is integrated in a box using the expansion of the time-dependent wave function  
 121  $\Psi(\mathbf{r}_1, \mathbf{r}_2, t)$  in a basis set consisting of eigenstates of the field-free atomic Hamiltonian  $H$ :

$$\Psi(\mathbf{r}_1, \mathbf{r}_2, t) = \sum_{L=0}^{L_{\max}} \sum_{n=1}^{N_L} c_{Ln}(t) \Phi_{Ln}(\mathbf{r}_1, \mathbf{r}_2), \quad (9)$$

122 where  $\Phi_{Ln}(\mathbf{r}_1, \mathbf{r}_2)$  denotes the  $n^{\text{th}}$  eigenfunction of  $H$  having total angular momentum  $L$  and  
 123 corresponding to the real “box” eigenenergy  $\epsilon_{Ln}$ :

$$H\Phi_{Ln}(\mathbf{r}_1, \mathbf{r}_2) = \epsilon_{Ln}\Phi_{Ln}(\mathbf{r}_1, \mathbf{r}_2). \quad (10)$$

124 The expansion (9) includes  $N_L$  eigenstates for the angular momentum  $L$ , and it includes all  
 125 the angular momenta up to  $L_{\max}$ . The basis set used in the variational calculations of the  
 126 field-free eigenstates  $\Phi_{Ln}(\mathbf{r}_1, \mathbf{r}_2)$  consists of  $LS$ -coupled independent-particle basis functions.  
 127 Antisymmetric two-electron basis functions coupled to form a state of definite  $S$ ,  $L$ , and  
 128 parity  $P$  are constructed in terms of one-electron orbitals (2) as explained in Refs. [18, 19].  
 129 The radial one-electron wave functions  $\varphi_{jl}(r)$  are obtained by solving Eq. (2) in a radial box  
 130 of size  $r_0 > r_b$  with boundary conditions  $\varphi_{jl}(0) = \varphi_{jl}(r_0) = 0$  for both positive and negative  
 131 energies  $\epsilon$ . The index  $j$  denotes the number of nodes of the radial wave function inside the  
 132 box. Eq. (2) is solved by expansion of the radial orbitals in the basis set of  $B$ -splines [21]  
 133  $B_i^k(r)$  satisfying the bound-state boundary conditions:

$$\varphi_{jl}(r) = \sum_{i,k} c_{jlik} B_i^k(r). \quad (11)$$

134 The radial box is divided into several intervals (denoted by index  $k$ ) by knots and the  
 135  $B$ -splines are defined in terms of the knots in each interval.

136 Use of the *LS*-coupled basis as discussed above is nowadays a standard technique fre-  
 137 quently employed in the theoretical treatment of both time-dependent [19, 21, 22] and  
 138 time-independent [18] problems for two active electron atomic systems. The radial one-  
 139 electron orbitals are often expressed in terms of *B*-splines [19, 21, 22] or discrete variable  
 140 representation (DVR) basis sets [23].

141 In order to suppress the reflections from the outer boundary of the radial box in the  
 142 solution of the TDSE (4) and to keep its size reasonably small, the CAP term (8) is added  
 143 to the Hamiltonian used for the time-propagation. The presence of this term makes the  
 144 total Hamiltonian of the system a complex symmetric rather than hermitian operator [20].  
 145 One note should be made at this point regarding the form of the matrix elements of all the  
 146 operators used here. Since all the calculations are performed in the eigenrepresentation of the  
 147 field-free atomic Hamiltonian  $H$  not including the CAP, the operators  $H$ ,  $D_I(t)$  and  $D_X(t)$   
 148 have real matrix elements, as it is convenient in hermitian quantum mechanics.  $V_C$  is the only  
 149 non-hermitian term in the total Hamiltonian. Therefore, it is not necessary to distinguish the  
 150 standard hermitian scalar product and complex symmetric product throughout the present  
 151 work (see Ref. [24] and references therein for details).

152 Both laser pulses are linearly polarized along the  $z$ -axis, and of course the  $^1S^e$  ground state  
 153 of He has zero projection  $M_L$  of the total orbital angular momentum on the polarization  
 154 axis. Accordingly it is also enough to consider only the  $z$ -component of the dipole operator.  
 155 According to the selection rules for the matrix elements of the dipole moment operators  
 156  $(\mathbf{d}_z)_{LnL'n'} = \langle \Phi_{Ln} | z_1 + z_2 | \Phi_{L'n'} \rangle$ , these are non-zero only if  $L - L' = \pm 1$  [25].

157 Projection of the TDSE (4) on the eigenstates of the field-free Hamiltonian (10) yields  
 158 the following set of coupled differential equations of the first order:

$$i\dot{\mathbf{c}}(t) = [\mathbf{H} + \mathbf{V}_C + \mathbf{D}_I(t + t_D) + \mathbf{D}_X(t)] \mathbf{c}(t), \quad (12)$$

159 where  $\mathbf{c}(t)$  is the vector of expansion coefficients used in (9) and the matrices on the right  
 160 hand side are the representations of the corresponding operators in the basis set  $\Phi_{Ln}(\mathbf{r}_1, \mathbf{r}_2)$   
 161 introduced above. The dimension of this system of differential equations is  $N = \sum_{L=0}^{L_{\max}} N_L$ .  
 162 In the present representation  $\mathbf{H}$  is a real diagonal matrix of the field-free atomic eigenen-  
 163 ergies. Since  $V_C$  given by Eq. (8) has no angular dependence,  $\mathbf{V}_C$  is an imaginary and  
 164 symmetric block diagonal matrix with  $L_{\max} + 1$  non-zero blocks having dimensions  $N_L$ .  
 165  $\mathbf{D}_{I,X}(t)$  are real symmetric banded matrices with only non-zero blocks corresponding to the

166 coupling of the total angular momentum  $L$  with  $L \pm 1$ , because we only consider  $M_L = 0$   
 167 states in this study. The physical picture of the phenomenon studied here suggests that the  
 168 IR dressing laser pulse couples the singlet autoionizing states  $2s2p$  ( $^1P^o$ ),  $2p^2$  ( $^1S^e$ ) and the  
 169 continuum states made accessible by the IR pulse. The energy difference between the ground  
 170 state and the lowest odd-parity, singlet excited state -  $1s2p$  ( $^1P^o$ ) of the field-free atom is so  
 171 high that it requires more than 18 photons to be absorbed to excite the ground state by  
 172 the IR pulse. Transitions of higher orders would thus be necessary to excite higher excited  
 173 states directly from the IR pulse acting on the ground state. Therefore, it is a reasonable  
 174 assumption to neglect the IR coupling of the ground state with excited states. Note that the  
 175 weak effect of the IR field for intensities considered in this work is also suggested in Ref. [26].  
 176 Therefore, the matrix elements of the dipole operator in the interaction matrix for the IR  
 177 field  $(\mathbf{d}_z^I)_{00L'n'}$  were explicitly set to zero (considering the ground state the first element in  
 178 the basis set). This assumption allows for a dramatic improvement in the convergence of the  
 179 solutions of the TDSE with respect to the size of the basis set. On the other hand, it is the  
 180 primary role of the XUV probe laser pulse to couple the ground state with the autoionizing  
 181 state  $2s2p$  ( $^1P^o$ ) and with nearby continuum states. Since it has rather high photon energy  
 182 and low intensity (perturbative regime), it is unlikely that the XUV coupling between the  
 183 doubly-excited states and the continuum states will play any significant role. Therefore,  
 184 in the present study all the dipole matrix elements in the XUV interaction matrix  $\mathbf{D}_X(t)$   
 185 except those coupling to the ground state  $(\mathbf{d}_z^X)_{00L'n'}$ , are explicitly set to zero. Note that  
 186 a similar approximation for the XUV coupling in a similar context has been employed in  
 187 Ref. [5]. Using this approximation the system of coupled differential equations (12) can be  
 188 written as follows:

$$i\dot{\mathbf{c}}(t) = [\mathbf{H} + \mathbf{V}_C + E_I(t + t_D)\mathbf{d}_z^I + E_X(t)\mathbf{d}_z^X] \mathbf{c}(t). \quad (13)$$

190 The structure of the matrices is showed in Fig. 1. The atomic system is initially in the  
 191 ground state. Considering the ground state to be the first element of the basis set, the  
 192 initial condition can be written as  $c_{0,1}(t_0) = 1$ ,  $c_{L,n>1}(t_0) = 0$ . The neglect of the ground  
 193 state coupling with the other field-free eigenstates via the IR laser pulse allows for reduction  
 194 of the total interval for the propagation of the TDSE as well. Since  $\tau_I > \tau_X$ , it would be  
 195 necessary to start the propagation of the TDSE (12) in the time  $t_0 = -t_D - \tau_I/2$ , if this  
 196 assumption were not made. It would also then be necessary to perform the propagation of



$$i \frac{d}{dt} \begin{pmatrix} 0 \\ 0 \\ \vdots \\ 0 \end{pmatrix} = \left[ \begin{array}{c} \boxed{\begin{array}{c} \text{grey blocks} \\ \mathbf{H} + \mathbf{V}_C \end{array}} + E_I(t + t_D) \boxed{\begin{array}{c} \text{grey blocks} \\ \mathbf{d}_z^I \end{array}} + E_X(t) \boxed{\begin{array}{c} \text{grey blocks} \\ \mathbf{d}_z^X \end{array}} \right] \begin{pmatrix} 0 \\ 0 \\ \vdots \\ 0 \end{pmatrix}$$

FIG. 1. Structure of the matrices in the system of coupled equations (13)

. The grey areas denote the non-zero blocks corresponding to definite total angular momenta and their dipole coupling. Matrix  $\mathbf{d}_z^I$  has zero first line and first column, while matrix  $\mathbf{d}_z^X$  has non-zero only the first row and column.

197 the wave function until the time  $t_1 = \max\{-t_D + \tau_I/2, \tau_X/2\}$ . Although the total wave  
 198 function described by the vector  $\mathbf{c}(t)$  changes at times  $t > t_1$  due to the presence of the  
 199 CAP, the population of the ground state will remain constant after the end of the pulses,  
 200 since the ground state wave function is well localized in the region where the CAP is zero.  
 201 Therefore, for the purpose of the present project it is enough to perform the propagation  
 202 until  $t_1$  and extract the population of the ground state  $c_{0,1}(t_1)$ . The approximation that  
 203 the IR field does not affect the ground state allows for the start of the propagation at time  
 204  $t_0 = -\tau_X/2$  and terminate it at time  $t_1 = \tau_X/2$ . In view of the long duration of both pulses,  
 205 this is an important simplification of the numerical calculations.

206 The method of solution of the TDSE used in the present work is based on the split  
 207 operator method in the basis set representation and it is described in the appendix in detail.  
 208 This represents an alternative approach to the higher-order quadrature methods [19, 27, 28]  
 209 frequently used in context of the interaction of atoms and molecules with strong laser fields.  
 210 Application of the split-operator technique is straightforward in case of the wave-packet  
 211 propagation (for details see Ref. [29] and references therein). However, the exponential of  
 212 the time dependent operator remains a challenge in the basis set representation . Palacios  
 213 *et al.* [30] introduced an implementation in the DVR basis set which has properties that  
 214 allow for an efficient numerical calculation of these exponentials. In the implementation  
 215 used here these time-dependent exponentials are calculated in the diagonal representation  
 216 of the dipole operators, as is discussed in the Appendix.

217 The photoabsorption yields obtained from the solutions of the TDSE (13) together with  
 218 the static photoabsorption yield enable a calculation of the transient absorption spectra.  
 219 This allows to relate the theoretical results presented here with the experimental transient

220 absorption spectra published in Ref. [11].

### 221 **III. FIELD-FREE HAMILTONIAN AND STATIC PHOTOABSORPTION SPEC-** 222 **TRUM**

223 Although we have found that the eigenrepresentation of the atomic Hamiltonian  $H$  with-  
224 out the CAP is more practical for the solutions of the TDSE (13), it is useful to study the  
225 spectrum of the complex symmetric Hamiltonian  $H_C = H + V_C$ .

226 This representation allows for easier optimization of the CAP parameter  $\eta$  and of the size  
227 of the radial box  $r_0$ . The complex eigenenergies allow for a better insight into the structure  
228 of the discretized continuum and evaluate its quality for the solution of the full TDSE as  
229 well. The eigenfunctions  $\phi_{Ln}(\mathbf{r}_1, \mathbf{r}_2)$  of the complex symmetric operator  $H_C = H + V_C$  are  
230 given by the equation

$$H_C \phi_{Ln}(\mathbf{r}_1, \mathbf{r}_2) = E_{Ln} \phi_{Ln}(\mathbf{r}_1, \mathbf{r}_2), \quad (14)$$

231 where the indices  $L, n$  have identical meaning as in Eq. (10). The complex eigenenergies can  
232 be written as  $E_{Ln} = E_{Ln}^r - i\Gamma_{Ln}/2$ . They should reproduce well the energy positions  $E_{Ln}^r$   
233 and widths  $\Gamma_{Ln}$  of the 2s2p ( $^1P^o$ ) and 2p<sup>2</sup> ( $^1S^e$ ) autoionizing states for  $L = 0, 1$ . In addition,  
234 the density of the discretized continuum states must be sufficient to accurately describe the  
235 interaction between the autoionizing states and the continuum and to allow for converged  
236 calculation of the photoionization yield. These properties of the basis set are controlled by  
237 the size of the box  $r_0$ , the position of the absorbing boundary  $r_b$  and the strength of the  
238 CAP  $\eta$ , as is described in Ref. [20]. These parameters have been optimized in the present  
239 calculations to the values  $r_0 = 200$  a.u. and  $r_b = 150$  a.u. These values allow for a good  
240 representation of the complex eigenenergies of the autoionizing states, they yield negligible  
241 decay widths of the ground and low excited states, and they provide a sufficient number of  
242 continuum states above the ionization threshold. The radial box is spanned by 700  $B$ -splines  
243 of the sixth order. The  $LS$ -coupled expansion includes the single-particle partial waves up to  
244  $l = 19$ , every partial wave includes 200 radial orbitals (see Eq. (2)). In order to describe the  
245 autoionizing states of the interest properly, the CI expansions of the states with  $L = 0$  and  
246  $L = 1$  include the doubly-excited configurations, where both electrons can occupy orbitals  
247 with  $l \leq 6$  and  $j \leq 6$ . In the remaining configurations one electron is restricted to occupy  
248 a 1s, 2s, or 2p orbital, while the other electron can occupy any orbital, constrained so that

249 the configurations contribute to the states with given spin  $S$ , total angular momentum  $L$   
 250 and parity  $P$ . The higher partial waves  $l$  included in the expansion are required for the  
 251 representation of the continuum states having high total angular momentum  $L$ ; they are  
 252 essential for obtaining converged solutions of the full TDSE including the nonperturbative  
 253 IR laser pulse. Optimization of the parameter  $\eta$  as is described in the Ref. [20] using this basis  
 254 set yields the value  $\eta = 10^{-4}$ . The complex energies of the autoionizing states calculated  
 255 using the basis set presented here are compared with previously published experimental  
 256 results [16, 17] in Table I. The widths of both autoionizing states calculated here are in good

TABLE I. Comparison of the positions and widths of the  $2s2p$  ( $^1P^o$ ) and  $2p^2$  ( $^1S^e$ ) doubly-excited states calculated from diagonalization of the Hamiltonian  $\mathbf{H}_C$  presented in this work with experimental values. The value  $\eta = 10^{-4}$  was used for the CAP parameter. The positions are relative to the ground state  $1s^2$ . The values in brackets are obtained by fitting the perturbation calculations to the Fano line-shape.

|                    | Position (eV)       |            | Width (eV)          |             |
|--------------------|---------------------|------------|---------------------|-------------|
|                    | Present calculation | Experiment | Present calculation | Experiment  |
| $2s2p$ ( $^1P^o$ ) | 59.687 (59.688)     | 60.15 [16] | 0.0411 (0.0456)     | 0.0373 [16] |
| $2p^2$ ( $^1S^e$ ) | 61.747              | 62.06 [17] | 0.0063              | 0.0059 [17] |

257  
 258

259 agreement with the experimental results. The discrepancies in their relative positions with  
 260 respect to the ground state are mainly due to the inaccurate representation of the  $1s^2$  ground  
 261 state by our truncated atomic Hamiltonian  $\mathbf{H}$ . It gives a computed ground state energy of  
 262  $E_{1s^2} = -2.88343$  a.u., while the accurate experimental value is  $E_{1s^2}^{\text{EXP}} = -2.90378$  a.u. [31].  
 263 To improve the ground state energy (and subsequently the relative positions of the double  
 264 excited states) a significantly larger basis set would be necessary. However, the difference of  
 265 doubly-excited state energies is more important for the calculations of the photoabsorption  
 266 spectra than their relative position with respect to the ground state. As can be seen from  
 267 Table I, the energy difference according to the calculations is  $\Delta E = 2.06$  eV, while the  
 268 experimental results give  $\Delta E^{\text{EXP}} = 1.91$  eV.

269 The distribution of the  $^1S^e$  and  $^1P^o$  continuum states in the complex energy domain is  
 270 plotted in Fig. 2. The IR laser pulse assumed here allows for the optical field ionization of

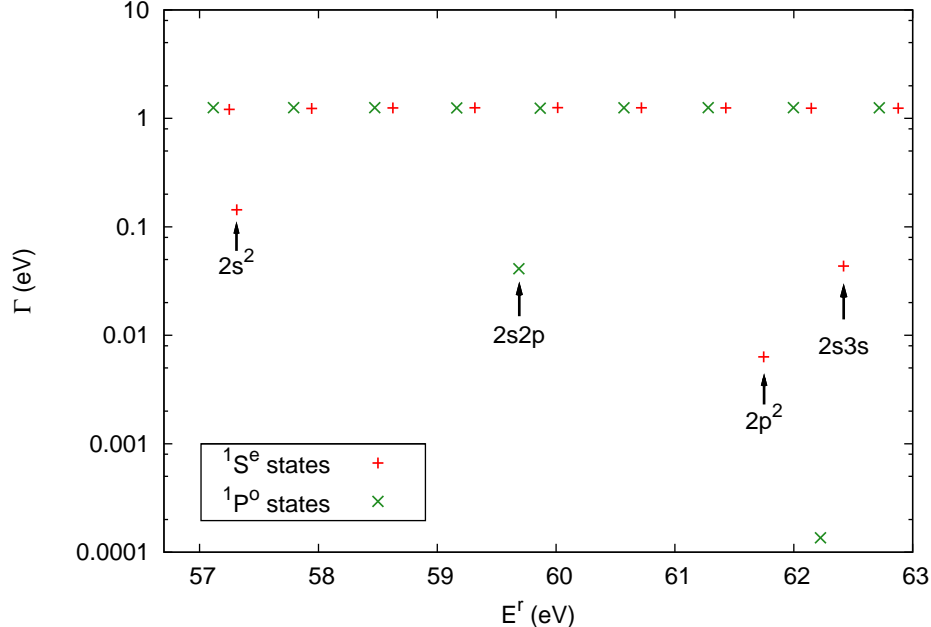
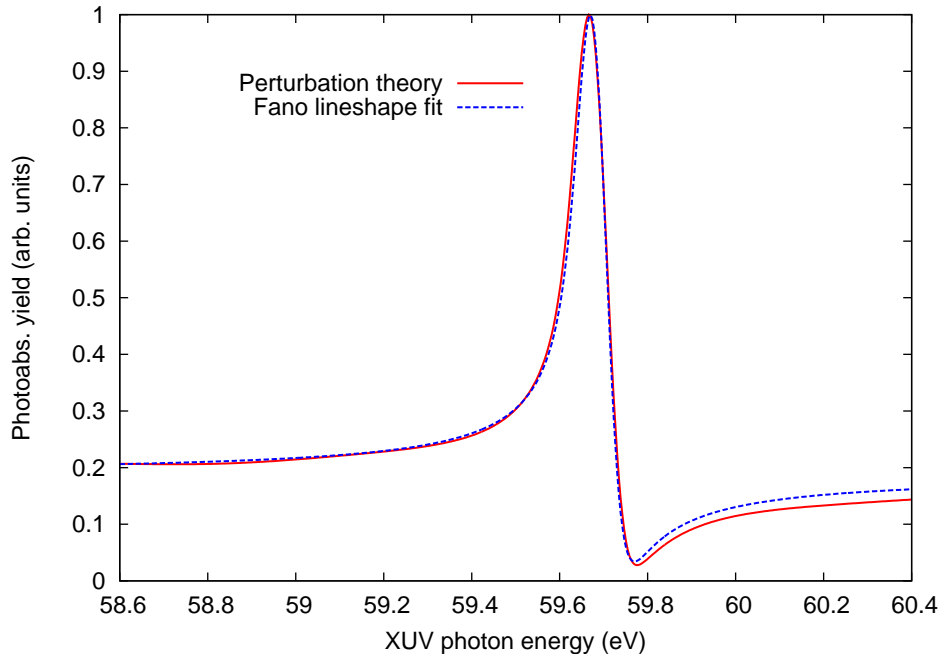


FIG. 2. (Color online) Complex eigenenergies of the complex symmetric field-free Hamiltonian  $\mathbf{H}_C$  spanning the interval of energies probed by the XUV laser pulse. Energies of states with the total angular momentum  $L = 0$  and  $L = 1$  are plotted. The autoionizing states are labeled by their principal independent particle CI configurations. The autoionizing state with energy 62.22 eV without label does not have a single dominant CI configuration, its discrete component is a linear combination of the 2s3p and 3s2p configurations. The  $N = 2$  ionization threshold is at energy 64.86 eV.

271 the doubly-excited states into the  $N = 2$  continuum. Since Loh *et al.* [11] suggested that  
 272 inclusion of this effect is important for the proper treatment of the phenomenon studied  
 273 here, it is important to have a sufficiently high density of continuum states with higher total  
 274 angular momenta  $L$  in the energy range above the  $N = 2$  ionization threshold. Present  
 275 calculations of the dipole matrix  $\mathbf{d}_z^I$  yields  $\mu_{ab} = 2.11$  a.u. for the matrix element coupling  
 276 the 2s2p ( $1P^o$ ) and 2p<sup>2</sup> ( $1S^e$ ) states. This is in a good agreement with previously published  
 277 value 2.17 a.u. obtained from the eigenchannel  $R$ -matrix calculations [11].  
 278

279 To understand the effect of the IR laser pulse it is a necessary prerequisite to calculate  
 280 the static photoabsorption spectrum in the absence of the dressing laser pulse. The static  
 281 photoabsorption yield corresponds to a Fano line-shape [10] across the known energy  $\omega_1$  of  
 282 the 2s2p ( $1P^o$ ) doubly-excited state with respect to the 1s<sup>2</sup> ground state, which has a known

FIG. 3. (Color online) Loss of the ground state population in the absence of the IR pulse and its comparison with the Fano line-shape convolved with the bandwidth of the pulse.



283 width  $\Gamma_1$  and value  $q_1$  of the Fano line-shape parameter. However, it is a stringent test of  
 284 our basis set quality and of the CAP used throughout this work to calculate this photoab-  
 285 sorption yield independently using the present Hamiltonian and compare the corresponding  
 286 spectrum with previously published results [11]. This can be done by setting  $E_I^0 = 0$  in  
 287 Eq. (13). Taking into account the low intensity of the XUV laser field, it is most tractable  
 288 to calculate the static photoabsorption spectrum using time-dependent perturbation theory.  
 289 The corresponding loss of population of the ground state is shown in Fig. 3. This curve  
 291 should correspond to the convolution of the Fano line-shape with the the XUV laser pulse  
 292 bandwidth. Therefore, we have fitted the absorption yield obtained from the perturbation  
 293 calculations to this convolution and extracted the position, width and line-shape parameter  
 294 of the  $2s2p$  ( $^1P^o$ ) autoionizing state. The fitting procedure assumes a gaussian envelope of  
 295 the laser pulse with bandwidth 0.06 eV (FWHM). The values for position and width obtained  
 296 from the fitting are compared with previously published results in Table I. As expected,  
 297 they agree very well with the values obtained from diagonalization of  $\mathbf{H}_C$ . In addition, the  
 298 fitting procedure yields  $q_1 = -2.71$ , in good correspondence with the value -2.75 published  
 299 in Ref. [11]. The convolved Fano line-shape corresponding to the fitted parameters is also  
 300 shown in Fig. 3. The good correspondence between the perturbation calculations (using the

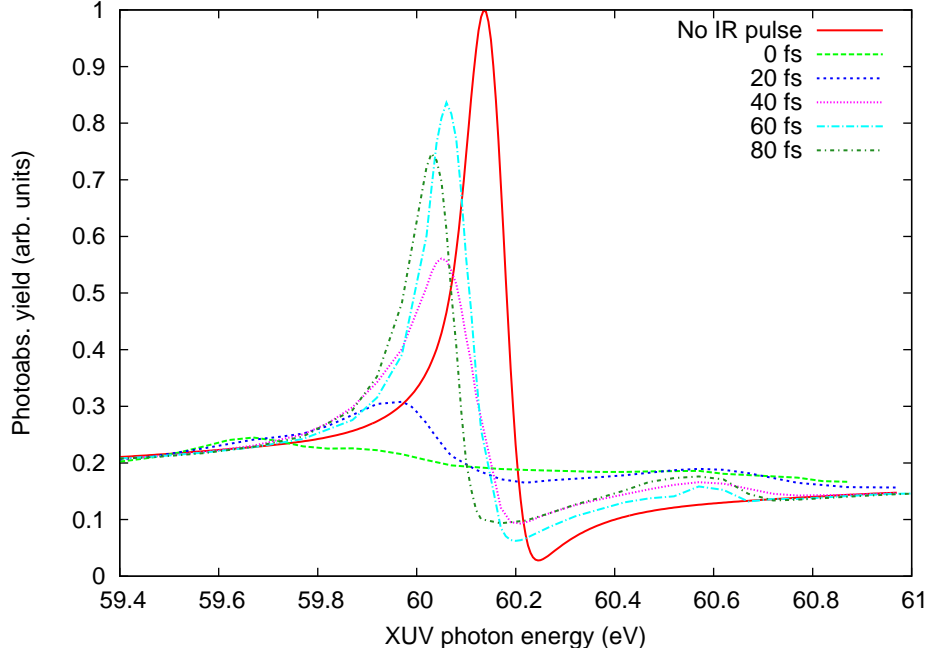


FIG. 4. (Color online) Loss of the ground state population for several time delays as a function of the XUV photon energy calculated for the IR laser pulse with  $\lambda_{\text{IR}} = 800 \text{ nm}$  and peak intensity  $I_I^0 = 1.4 \times 10^{13} \text{ W/cm}^2$

301  $\cos^2$  XUV pulse envelope) and the Fano line-shape fit convolved with the gaussian function  
 302 suggests that the results are not sensitive to the details of the XUV pulse envelope.

#### 303 IV. PHOTOABSORPTION BY THE DRESSED HELIUM ATOM

304 The loss of the ground state population at the end of the probe pulse  $p(\omega_X) = 1 - |c_{00}(t_1)|^2$   
 305 calculated from Eq. (13) as a function of the XUV photon energy  $\omega_X$  for several time delays  
 306  $t_D$  is shown in Fig. 4. Since the duration of the dressing laser pulse is longer than the  
 308 duration of the XUV pulse, different intensities of the IR field are probed at different time  
 309 delays  $t_D$ . As can be seen in Fig. 4, the Fano line-shape disappears in the case of the perfect  
 310 overlap of both pulses and the photoabsorption yield becomes essentially structureless. The  
 311 peak and the minimum shifted with respect to the static case become more pronounced  
 312 with increasing time delay  $t_D$ . An additional peak appears around the XUV photon energy  
 313 60.6 eV for  $t_D > 0 \text{ fs}$ . Its energy position does not change significantly with changing time  
 314 delay. Loh *et al.* [11] performed a model calculation of the photoabsorption yield based on

315 the three-level model developed in Ref. [15] describing the Autler-Townes doublet formation.  
 316 It explains the presence of the additional peak in the photoabsorption yield as well as the  
 317 shift of the higher peak with respect to the static case. The Ref. [11] model calculations  
 318 that include optical field ionization of the doubly-excited states into the  $N = 2$  continuum  
 319 due to the IR field confirm that this effect leads to a significant line-width broadening. This  
 320 broadening makes the Autler-Townes doublet nearly invisible and the position of the peak  
 321 at positive XUV detunings hardly shifts as the IR pulse intensity is changed. Since the  
 322 calculations presented in this work were performed at an intensity that allows for optical  
 323 field ionization, our results are in good correspondence with the theoretical considerations  
 324 presented in Ref. [11].

325 The present calculations account for the time profile of both pulses, whereby the pho-  
 326 toabsorption yields shown in Fig. 4 together with the static photoabsorption yield plotted in  
 327 Fig. 3, enable a calculation of the transient absorption spectra that can be compared with  
 328 experimental results published in [11].

329 The change of the optical density  $\Delta OD$  is calculated using the formula that takes into  
 330 account the energy resolution of the spectrometer used in the experiment [11]:

$$\Delta OD(\omega_X) = -\log_{10} \frac{\int \exp \left[ -\sigma(\omega) n_t \ell - \frac{4 \ln 2}{\Delta \omega^2} (\omega - \omega_X)^2 \right] d\omega}{\int \exp \left[ -\sigma_0(\omega) n_t \ell - \frac{4 \ln 2}{\Delta \omega^2} (\omega - \omega_X)^2 \right] d\omega}, \quad (15)$$

331 where  $\sigma(\omega)$  and  $\sigma_0(\omega)$  are the photoabsorption cross section of the dressed medium and  
 332 static photoabsorption cross section in the absence of the IR pulse, respectively.  $n_t$  is the  
 333 atom number density of the helium gas in the tube and  $\ell$  is the length of the tube in  
 334 the direction parallel to the direction of laser propagation.  $\Delta \omega = 0.18 \text{ eV}$  is the energy  
 335 resolution of the spectrometer (FWHM) used in the experiment [11]. Determination of the  
 336 photoabsorption cross section from the photoionization yield obtained from Eq. (13) is not  
 337 straightforward. The usual relation between the single-photon absorption cross section and  
 338 the photoabsorption rate (probability per photon per second)  $dp/dt$  for an infinitely long  
 339 monochromatic pulse with photon energy  $\omega$  is given by the formula

$$\sigma(\omega) = \frac{dp(\omega)}{dt} \frac{\omega}{I}, \quad (16)$$

340 where  $dp/dt$  is the photoabsorption rate as a function of the photon energy  $\omega$  and  $I$  is the  
 341 corresponding light intensity. This formula assumes that the photoabsorption rate does not  
 342 depend on time. The situation in the present work is more complicated. Both pulses have

343 a finite duration, and the photoabsorption rate varies with time. This time dependence  
 344 should be included in Eq. (16). However, when one takes into account other assumptions  
 345 made regarding the shape of the XUV pulse, it is a good approximation to calculate the  
 346 photoabsorption cross section using the formula

$$\sigma(\omega_X) = A \frac{p(\omega_X)\omega_X}{T_X I_X}, \quad (17)$$

347 where  $p(\omega_X)$  is the photoabsorption probability obtained from Eq. (13),  $T_X$  is the duration  
 348 of the XUV pulse and  $I_X$  is the corresponding XUV pulse intensity used to calculate  $p(\omega_X)$ .  
 349 The scaling factor  $A$  approximately accounts for the time dependence of the XUV field  
 350 intensity and of the photoabsorption rate. Its value was chosen so that the calculated  
 351 absorption spectra reproduce well the experimental transient absorption spectra published  
 352 in Ref. [11]. Since  $A$  is related to the XUV pulse only, the value used to calculate the  
 353 static optical density is the same as the value used to calculate the optical density in the  
 354 presence of the IR field. The comparison between our theoretical results and the Ref. [11]  
 355 experiment is presented in Fig. 5. The best correspondence between the present calculations  
 357 and experimental results was achieved by setting  $A = 3.5$  for the time delays  $t_D = 0$  fs, 20 fs  
 358 and 40 fs. The remaining spectra with time delays  $t_D = 60$  fs and 80 fs compare best with the  
 359 experimental results for  $A = 5$ . Therefore, the best fit of the experimental data is obtained  
 360 when the product  $I_X T_X$  used in the calculations is smaller than the values estimated in the  
 361 experimental work [11]. The calculated transient absorption spectra plotted in Fig. 5 have  
 362 been shifted on the energy axis by 0.45 eV to correct for the inaccuracy of the 2s2p ( $^1P^o$ )  
 363 doubly-excited state position with respect to the ground state in the present calculations (see  
 364 Table I and the discussion in Sec. III). A change of the value of the parameter  $A$  affects the  
 365 ratio of the peak magnitudes in the transient absorption spectra, however it does not affect  
 366 the positions of the structures in the curves. As can be seen in Fig. 5, the present theoretical  
 367 calculations are generally in encouraging agreement with the experimental results. The left  
 368 peak that develops with increasing time delay is a consequence of the rising maximum of  
 369 the photoabsorption spectrum due to decreasing IR intensities probed by the XUV pulse.  
 370 The figure shows that this peak develops in the present calculations more rapidly with  
 371 increasing time delay than is evident in the experimental results. The peak at positive XUV  
 372 detunings calculated in the present study corresponds well to the experimental results. Since  
 373 the probe pulse is produced by the HHG, it is expectable that its spatial and frequency



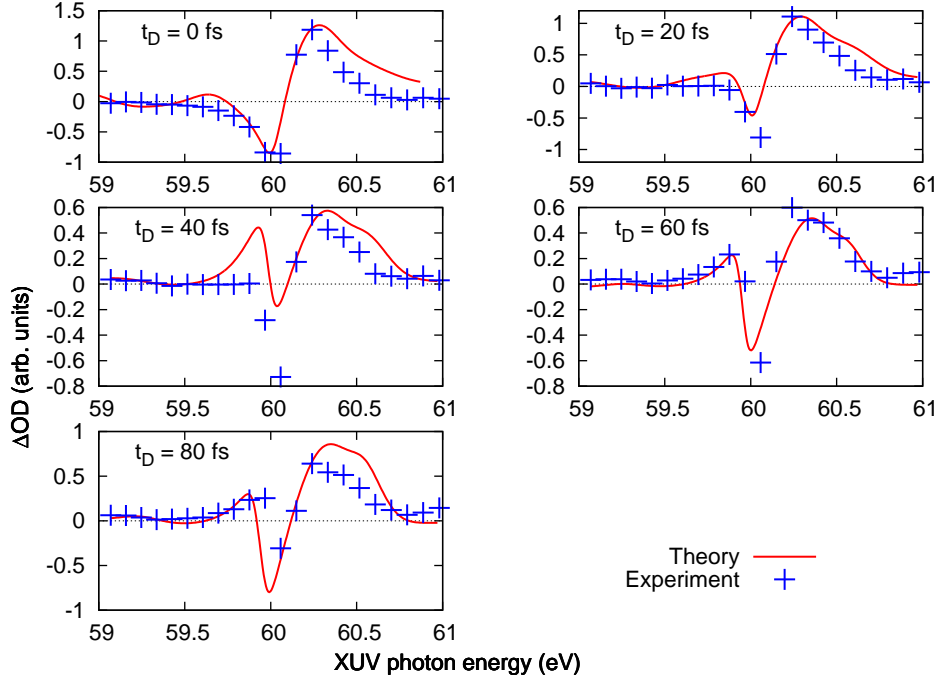


FIG. 5. (Color online) Transient absorption spectra calculated using Eq. (15) for different time delays  $t_D$  and their comparison with experimental results [11]. The value of the scaling constant  $A = 3.5$  was used to calculate the spectra with time delays 0 fs, 20 fs and 40 fs. The value  $A = 5$  was used to calculate the spectra with time delays 60 fs and 80 fs.

374 profile have more difficult structure than a simple gaussian envelope as it is assumed in this  
 375 work. Therefore, the discrepancies between the experimental transient absorption spectra  
 376 published in Ref. [11] and the spectra presented here can possibly be attributed to the  
 377 simplified shape of the XUV pulse assumed in the present theoretical treatment.

378 Although the photoabsorption yields in Fig. 4 show the reduced XUV photon absorption  
 379 caused by the dressing IR laser pulse, the relation between these results and the EIT-like  
 380 structures is not straightforward. The spectral peaks corresponding to the dressed states  
 381 of the Autler-Townes doublet approach each other linearly as the Rabi splitting  $\Omega_c$  of the  
 382 states coupled by the IR laser pulse decreases. This behavior is not apparent in Fig. 4.  
 383 The Rabi splittings  $\Omega_c$  probed by the peak of the XUV laser pulse at time delays  $t_D = 0$  fs,  
 384 20 fs and 40 fs are  $\Omega_c = 1.18$  eV, 0.62 eV and 0.0025 eV, respectively. The splitting for larger  
 385 time delays  $t_D$  is significantly smaller than the width of the  $2s2p$  ( $^1P^o$ ) doubly-excited state.  
 386 However, Fig. 4 does not show any corresponding rapid change in the energy separation of

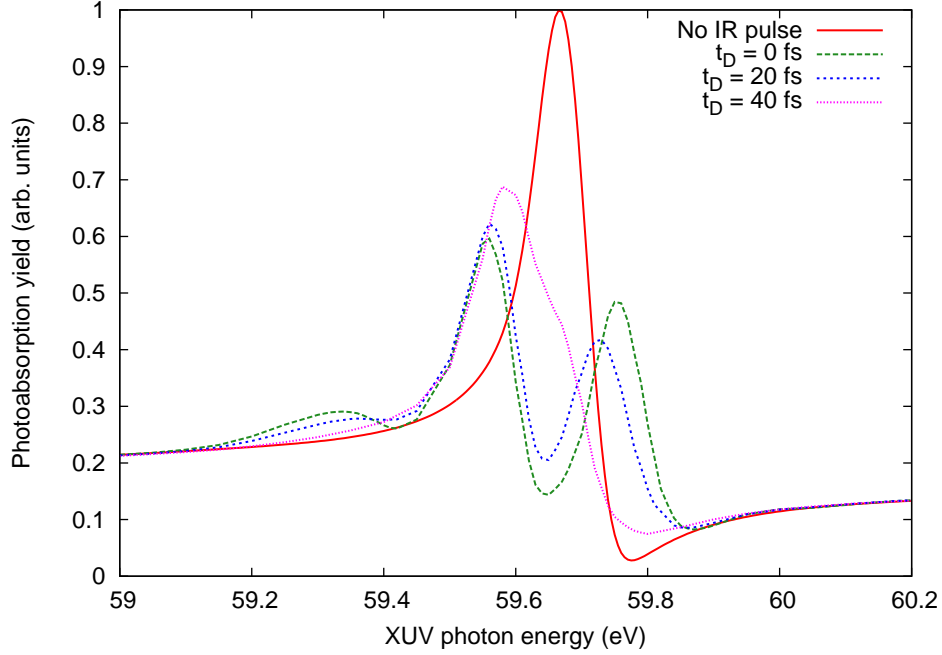


FIG. 6. (Color online) Photoabsorption yield calculated for the peak intensity of the IR field  $I_0 = 7 \times 10^{11} \text{ W/cm}^2$  and for the dressing pulse wavelength  $\lambda_I = 600 \text{ nm}$  corresponding to the energy difference between the  $2s2p$  ( $^1P^o$ ) and  $2p^2$  ( $^1S^e$ ) doubly-excited states. Curves for time delays  $t_D = 0 \text{ fs}$ ,  $20 \text{ fs}$   $40 \text{ fs}$  are compared with the static photoabsorption yield with no IR pulse

387 the peaks as the time delay is changed. The clear interpretation of these photoabsorption  
 388 yields is complicated by the optical field ionization of the doubly-excited states, by the  
 389 finite durations of the laser pulses, and by the large detuning of the dressing laser from the  
 390 energy difference of the  $2s2p$  ( $^1P^o$ ) and  $2p^2$  ( $^1S^e$ ) doubly-excited states. In order to eliminate  
 391 the effect of the large IR detuning, another calculation was performed with the wavelength  
 392 of the IR laser pulse modified to  $600 \text{ nm}$ . The corresponding photon energy  $2.06 \text{ eV}$  now  
 393 matches the calculated energy difference between the doubly-excited states  $2s2p$  ( $^1P^o$ ) and  
 394  $2p^2$  ( $^1S^e$ ) (see Table I). In order to suppress the effect of the optical field ionization, the peak  
 395 intensity of the coupling IR laser pulse was decreased to  $I_I^0 = 7 \times 10^{11} \text{ W/cm}^2$ . Corresponding  
 396 photoabsorption yields are shown in Fig. 6. This graph shows for  $t_D = 0 \text{ fs}$  two peaks with  
 398 energy separation  $0.2 \text{ eV}$  and minimum between them at energy close to the position of the  
 399 static photoabsorption peak. The Rabi splitting of the autoionizing states coupled by the  
 400 IR laser pulse with the reduced peak intensity used here is  $\Omega_c = 0.27 \text{ eV}$ . The curve for time  
 401 delay  $t_D = 20 \text{ fs}$  shows similar behavior. The energy separation of the peaks is  $0.16 \text{ eV}$ , the

402 Rabi splitting of the  $2s2p$  ( $^1P^o$ ) and  $2p^2$  ( $^1S^e$ ) doubly-excited states probed by the peak of  
 403 the XUV laser pulse is  $\Omega_c = 0.145$  eV. In case of larger time delay  $t_D = 40$  fs both peaks  
 404 have a strong overlap and their energy separation is smaller than the width of the  $2s2p$  ( $^1P^o$ )  
 405 doubly-excited state. This correspondence confirms that we can interpret these structures  
 406 as the Autler-Townes doublet. Energy separations of the peaks for single time delays  $t_D$   
 407 do not exactly match the corresponding Rabi splittings  $\Omega_c$ , mainly because of the finite  
 408 duration of both pulses. Another reason could be the coupling of additional doubly-excited  
 409 states by the IR laser pulse that would add further complications to the three-level picture.  
 410 The presence of an additional autoionizing state in the coupling scheme also appears to  
 411 explain the smallest additional peak at an energy below 59.4 eV which occurs at small time  
 412 delays in Fig. 6. The  $2s^2$  ( $^1S^e$ ) doubly-excited state is a good candidate, since the energy  
 413 difference between the  $2s^2$  ( $^1S^e$ ) and  $2s2p$  ( $^1P^o$ ) doubly-excited states is 2.373 eV in the  
 414 present calculations. In general, the calculations performed with the reduced IR intensity  
 415 and with the photon energy adjusted as discussed above show the EIT-like structure more  
 416 clearly than the calculations performed with parameters of the IR laser pulse used in the  
 417 experiment. This suggests that the Autler-Townes structure in the calculations carried out  
 418 using the experimental parameters are not very pronounced simply because the dressing  
 419 laser detuning is so large.

420 In order to investigate the manner in which the optical field ionization of the autoionizing  
 421 states affects the dressed photoabsorption spectra, another calculation with the adjusted  
 422 IR laser pulse ( $\lambda_I = 600$  nm) was performed. The experimental peak intensity of the IR  
 423 dressing laser pulse  $I_I^0 = 1.4 \times 10^{13}$  W/cm<sup>2</sup> was used. The resulting photoabsorption yields  
 424 for several time delays  $t_D$  are shown in Fig. 7. This graph shows a broad peak around  
 425 the energy 58.7 eV and a richer structure in the energy interval from 59.7 eV to 60.3 eV  
 426 in case of perfect temporal overlap of the two laser pulses. These structures approach  
 427 each other with increasing time delay  $t_D$ . Since optical field ionization broadens the line-  
 428 widths, the characterization of the individual peaks in the photoabsorption spectra is not  
 429 straightforward. However, the well pronounced separation of the broad peak at negative  
 430 XUV detuning and the structure at positive XUV detuning is most likely related to the  
 431 coupling of the  $2s2p$  ( $^1P^o$ ) and  $2p^2$  ( $^1S^e$ ) autoionizing states, as can be assumed from the  
 432 change of the separation with increasing time delay  $t_D$ . It is possible that the IR field  
 433 at the experimental peak intensity  $I_I^0 = 1.4 \times 10^{13}$  W/cm<sup>2</sup> enables coupling of additional  
 434

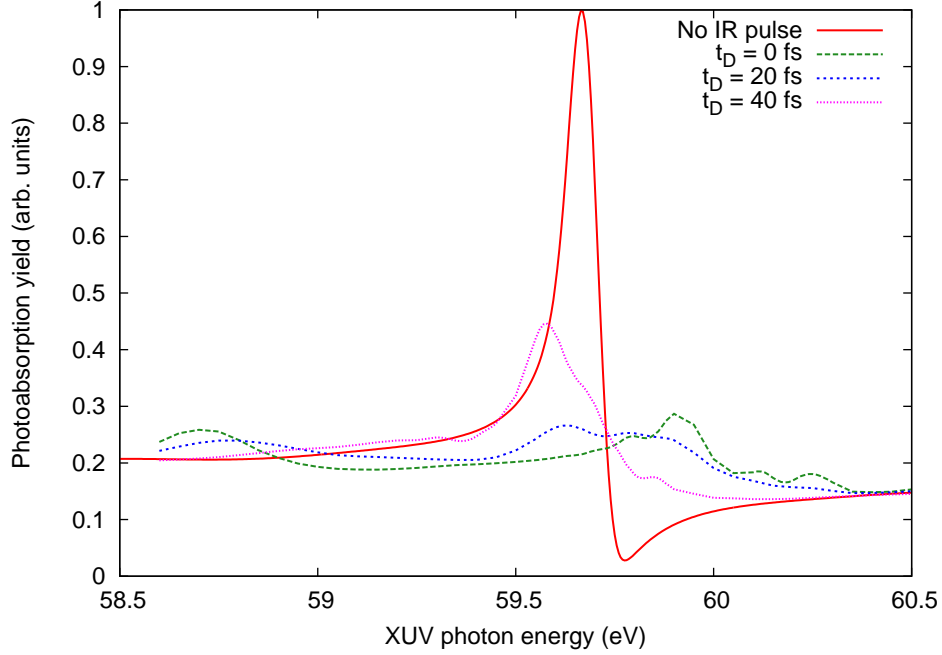


FIG. 7. (Color online) The photoabsorption yield calculated for the peak IR field intensity  $I_0 = 1.4 \times 10^{13} \text{ W/cm}^2$  and for the dressing pulse wavelength  $\lambda_I = 600 \text{ nm}$  corresponding to the energy difference between the  $2s2p$  ( $^1P^o$ ) and  $2p^2$  ( $^1S^e$ ) doubly-excited states. Curves for time delays  $t_D = 0 \text{ fs}$ ,  $20 \text{ fs}$ ,  $40 \text{ fs}$  are compared with the static photoabsorption yield.

435 autoionizing states and this coupling leads to the rich structure of peaks appearing at positive  
 436 XUV detunings.

## 437 V. CONCLUSIONS

438 This work presents theoretical treatment of the photoabsorption in XUV for helium  
 439 dressed by the IR laser. The  $2s2p$  ( $^1P^o$ ) and  $2p^2$  ( $^1S^e$ ) doubly-excited states are coupled by  
 440 strong  $800 \text{ nm}$  laser pulse with duration  $42 \text{ fs}$ . This system is probed by the weak XUV pulse  
 441 produced by HHG. The photoabsorption yields in the presence of both pulses are calculated  
 442 as a function of the XUV photon energy for several dressing-probe time delays by solving the  
 443 TDSE. The calculated transient absorption spectra are in reasonable correspondence with  
 444 experimental results of Loh *et al.* [11]. The presence of the coupling IR laser significantly  
 445 reduces the peak photoabsorption yield and changes of the time delay between the dressing  
 446 and probe pulse show the dependence on the IR field intensity that is probed by the XUV

447 photons. Calculations performed with the wavelength of the dressing laser modified to  
448  $\lambda_I = 600$  nm, corresponding to zero detuning of the IR laser, clearly show a structure in  
449 the photoabsorption spectrum that can be interpreted as the Autler-Townes doublet and an  
450 EIT-like structure. This allows us to conclude that this was not clearly pronounced in the  
451 experimental results published in Ref. Loh *et al.* [11] primarily because of the large detuning  
452 of the IR laser. The photoabsorption yields calculated for different dressing laser intensities  
453 showed that the optical field ionization of the doubly-excited states broadens the linewidths  
454 and increasing dressing laser intensity leads to formation of more complicated structures in  
455 the photoabsorption spectra. These could result from the increasing importance of additional  
456 autoionizing states at higher IR intensity.

457 The method of solution of the TDSE presented in this work proved to be stable and  
458 suitable for theoretical treatment of two active electron atoms in pump-probe settings of the  
459 laser pulses with a potential of further improvement in the future.

## 460 **ACKNOWLEDGMENTS**

461 Conversations with Zhi-Heng Loh and Stephen Leone are greatly appreciated, as is ac-  
462 cess to some of their unpublished data and calculations. We also thank Andreas Becker  
463 and Antonio Picón for stimulating discussions. This work was supported in part by the De-  
464 partment of Energy, Office of Science. This research used resources of the National Energy  
465 Research Scientific Computing Center, which is supported by the Office of Science of the  
466 U.S. Department of Energy.

## 467 **Appendix: Method of the solution of the TDSE**

468 Since it is necessary to integrate the system of equations (12) for a set of different XUV  
469 photon energies  $\hbar\omega_X$  and pump-probe time delays  $t_D$ , it is important to employ an integra-  
470 tion method that efficiently meets these requirements. After tests of several different meth-  
471 ods used elsewhere in similar contexts (e.g. Runge-Kutta [19] and Crank-Nicholson [29]) we  
472 chose to implement the split-operator technique [29] in a basis set representation. The basic  
473 idea of this propagation method is that if the total time-dependent Hamiltonian  $\mathbf{H}_T(t)$  can  
474 be written as a sum of the time-independent and time-dependent parts  $\mathbf{H}_T(t) = \mathbf{H}_0 + \mathbf{H}_1(t)$ ,

475 the propagation of the wave function between times  $t$  and  $t + \Delta t$ , where  $\Delta t$  is sufficiently  
 476 small, can be implemented to second order in the time step, as follows:

$$\Psi(t + \Delta t) = \exp\left(-\frac{i\Delta t}{2}\mathbf{H}_0\right) \exp\left[-i\int_t^{t+\Delta t}\mathbf{H}_1(t')dt'\right] \exp\left(-\frac{i\Delta t}{2}\mathbf{H}_0\right) \Psi(t) + \mathbf{O}\left[(\Delta t)^3\right]. \quad (\text{A.1})$$

477 If we denote

$$F_{I,X}(t, \Delta t) = \int_t^{t+\Delta t} E_{I,X}(t')dt', \quad (\text{A.2})$$

478 then the application of this method to the present system of equations (13) yields

$$\begin{aligned} \mathbf{c}(t + \Delta t) = \exp\left[-\frac{i\Delta t}{2}(\mathbf{H} + \mathbf{V}_C)\right] \exp\left[-i\mathbf{d}_z^I F_I(t + t_D, \Delta t) - i\mathbf{d}_z^X F_X(t, \Delta t)\right] \\ \exp\left[-\frac{i\Delta t}{2}(\mathbf{H} + \mathbf{V}_C)\right] \mathbf{c}(t) + \mathbf{O}\left[(\Delta t)^3\right]. \end{aligned} \quad (\text{A.3})$$

479 The first and third exponential terms in this equation can be calculated rather easily, as they  
 480 are time independent (for a fixed time step  $\Delta t$ ) and all the matrices are block diagonal. Since  
 481 the eigenrepresentation of the field-free Hamiltonian  $H$  is used, this term can be expressed  
 482 using the Crank-Nicholson formula

$$\exp\left[-\frac{i\Delta t}{2}(\mathbf{H} + \mathbf{V}_C)\right] = \frac{\mathbf{1} - i(\mathbf{H} + \mathbf{V}_C)\Delta t/4}{\mathbf{1} + i(\mathbf{H} + \mathbf{V}_C)\Delta t/4} + \mathbf{O}\left[(\Delta t)^3\right], \quad (\text{A.4})$$

483 which is accurate to second order in the time step. Although the evaluation of this term  
 484 requires a matrix inversion, it is not demanding, as it can be performed independently for  
 485 every block matrix corresponding to a definite angular momentum  $L$ . In addition, it is  
 486 necessary to perform this step only once before calculating the time propagation, as this  
 487 term is time independent.

488 Calculation of the second exponential in Eq. (A.3) is more difficult, as it explicitly depends  
 489 on time and is not block diagonal. Since  $\mathbf{d}_z^I$  and  $\mathbf{d}_z^X$  do not commute (see the structure in  
 490 Fig. 1), we can write this term using the split-operator formula (A.1) as follows:

$$\begin{aligned} \exp\left[-i\mathbf{d}_z^I F_I(t + t_D, \Delta t) - i\mathbf{d}_z^X F_X(t, \Delta t)\right] = \exp\left[-\frac{i}{2}\mathbf{d}_z^I F_I(t + t_D, \Delta t)\right] \\ \exp\left[-i\mathbf{d}_z^X F_X(t, \Delta t)\right] \exp\left[-\frac{i}{2}\mathbf{d}_z^I F_I(t + t_D, \Delta t)\right] + \mathbf{O}\left[(\Delta t)^3\right]. \end{aligned} \quad (\text{A.5})$$

491 The most straightforward way to calculate these exponentials is using the eigenrepresenta-  
 492 tions of  $\mathbf{d}_z^I$  and  $\mathbf{d}_z^X$ :

$$\begin{aligned} \exp\left[-i\mathbf{d}_z^I F_I(t + t_D, \Delta t) - i\mathbf{d}_z^X F_X(t, \Delta t)\right] = \mathbf{U}_I \text{diag}\left\{\exp\left[-\frac{i\lambda_k^I}{2}F_I(t + t_D, \Delta t)\right]\right\} \mathbf{U}_I^T \\ \mathbf{U}_X \text{diag}\left\{\exp\left[-i\lambda_k^X F_X(t, \Delta t)\right]\right\} \mathbf{U}_X^T \mathbf{U}_I \text{diag}\left\{\exp\left[-\frac{i\lambda_k^I}{2}F_I(t + t_D, \Delta t)\right]\right\} \mathbf{U}_I^T. \end{aligned} \quad (\text{A.6})$$

493 where  $\lambda_k^{I,X}$  are the eigenvalues of  $\mathbf{d}_z^{I,X}$  and  $\mathbf{U}_{I,X}$  are the corresponding matrices of the column  
 494 eigenvectors. Substitution of this result together with Eq. (A.4) into Eq. (A.3) and denoting

$$\mathbf{V}_1 = \mathbf{U}_I^T \frac{\mathbf{1} - i(\mathbf{H} + \mathbf{V}_C) \Delta t/4}{\mathbf{1} + i(\mathbf{H} + \mathbf{V}_C) \Delta t/4} \mathbf{U}_I, \quad \mathbf{V}_2 = \mathbf{U}_I^T \mathbf{U}_X, \quad \mathbf{c}_I(t) = \mathbf{U}_I^T \mathbf{c}(t) \quad (\text{A.7})$$

495 yields

$$\begin{aligned} \mathbf{c}_I(t + \Delta t) = \mathbf{V}_1 \text{diag} \left\{ \exp \left[ -\frac{i\lambda_k^I}{2} F_I(t + t_D, \Delta t) \right] \right\} \mathbf{V}_2 \text{diag} \left\{ \exp \left[ -i\lambda_k^X F_X(t, \Delta t) \right] \right\} \mathbf{V}_2^T \\ \text{diag} \left\{ \exp \left[ -\frac{i\lambda_k^I}{2} F_I(t + t_D, \Delta t) \right] \right\} \mathbf{V}_1^T \mathbf{c}_I(t). \end{aligned} \quad (\text{A.8})$$

496 This propagation scheme in one time step means that the wave function is first expressed in  
 497 the eigenrepresentation of  $\mathbf{d}_z^I$  and propagation for a quarter of the time step is performed us-  
 498 ing the field-free Hamiltonian augmented by the CAP. Then the wave function is propagated  
 499 in the IR field for half of the time step. After that the wave function is transformed into the  
 500 eigenrepresentation of the XUV dipole operator and the propagation for one time step is  
 501 performed in the XUV field only. The wave function is transformed back to the IR eigenrep-  
 502 resentation again and the propagation steps in the IR field only as well as the step using the  
 503 field-free Hamiltonian are performed. This propagation scheme involves only two matrices  
 504 which are time dependent and they are diagonal in different representations. It means that  
 505 only two changes of representation are necessary in every time step. Note that application  
 506 of Eq. (A.8) in two subsequent time steps allows for multiplication by the matrix  $\mathbf{V}_1^T \mathbf{V}_1$   
 507 between the steps. Therefore, every propagation step involves three matrix-vector multipli-  
 508 cations and two diagonal matrix-vector multiplications, where only the diagonal matrices  
 509 are time dependent. The matrix  $\mathbf{V}_2$  is real and the matrix  $\mathbf{V}_1^T \mathbf{V}_1$  is complex symmetric.  
 510 After the transformation of the initial state vector  $\mathbf{c}(t_0)$  from the energy eigenrepresentation  
 511 of  $\mathbf{H}$  to the diagonal representation of  $\mathbf{d}_z^I$ , the rest of the propagation is performed in this  
 512 basis. This approach is permissible in the context of the problem studied here, because we  
 513 only need to determine the depletion of the field-free ground state at the end of the XUV  
 514 laser pulse only, rather than information about the evolution of the complete wave function  
 515 during the pulse. Note that only the function  $F_X(t, \Delta t)$  depends on the XUV photon energy  
 516  $\hbar\omega_X$  and the information about the time delay  $t_D$  appears only in the diagonal matrix in  
 517 Eq. (A.8). Therefore, the same matrices  $\mathbf{V}_1^T \mathbf{V}_1$  and  $\mathbf{V}_2$  can be used in all the time dependent  
 518 calculations for all the values of  $\hbar\omega$  and  $t_D$  of interest.

519 One more note related to Eq. (A.5) should be made at this point. The split operator  
520 method is used there to calculate the exponential involving matrices  $\mathbf{d}_z^I$  and  $\mathbf{d}_z^X$  which do  
521 not commute. The non-zero commutator is a consequence of the approximation introduced  
522 in Sec. II, where we neglect the effect of the IR laser field on the ground state and neglect the  
523 XUV couplings that do not involve the ground state (see Fig. 1). Validity of this approxima-  
524 tion implies that the commutator  $[\mathbf{d}_z^I, \mathbf{d}_z^X]$  is sufficiently small to write the exponential on  
525 the left hand side of Eq. (A.5) simply as a product of two exponentials. This would change  
526 the form of the final time propagator (A.8) in such way that it will contain only two time-  
527 dependent matrices. Therefore, this approach would save one matrix-vector multiplication  
528 in every time step. However, its impact on the accuracy of the time propagation needs to  
529 be tested and its implementation will be the subject of forthcoming research.

530 In conclusion, the time required to calculate the matrices  $\mathbf{V}_1^T \mathbf{V}_1$  and  $\mathbf{V}_2$  (matrix diag-  
531 onalization, inversion and the matrix-matrix multiplication) is negligible compared to the  
532 calculations of the time propagation using Eq. (A.8). This propagation scheme is of the  
533 second order in the time step and scales as  $N^2$  with the dimension of the basis set used  
534 (since it involves only matrix-vector multiplications in every time step).

- 
- 535 [1] C. Cohen-Tannoudji and D. Guery-odelin, *Advances In Atomic Physics: An Overview* (World  
536 Scientific, 2011).
- 537 [2] S. E. Harris, J. E. Field, and A. Imamoglu, *Phys. Rev. Lett.* **64**, 1107 (1990).
- 538 [3] M. Fleischhauer, A. Imamoglu, and J. P. Marangos, *Rev. Mod. Phys.* **77**, 633 (2005).
- 539 [4] M. D. Lukin, *Rev. Mod. Phys.* **75**, 457 (2003).
- 540 [5] M. Wickenhauser, J. Burgdörfer, F. Krausz, and M. Drescher,  
541 *Phys. Rev. Lett.* **94**, 023002 (2005).
- 542 [6] H. Wang, M. Chini, S. Chen, C.-H. Zhang, F. He, Y. Cheng, Y. Wu, U. Thumm, and  
543 Z. Chang, *Phys. Rev. Lett.* **105**, 143002 (2010).
- 544 [7] L. Argenti and E. Lindroth, *Phys. Rev. Lett.* **105**, 053002 (2010).
- 545 [8] H. Bachau, P. Lambropoulos, and R. Shakeshaft, *Phys. Rev. A* **34**, 4785 (1986).
- 546 [9] S. I. Themelis, P. Lambropoulos, and M. Meyer,  
547 *J. Phys. B: At. Mol. Opt. Phys.* **37**, 4281 (2004).



- 548 [10] U. Fano, Phys. Rev. **124**, 1866 (1961).
- 549 [11] Z.-H. Loh, C. H. Greene, and S. R. Leone, Chem. Phys. **350**, 7 (2008).
- 550 [12] C. Buth, R. Santra, and L. Young, Phys. Rev. Lett. **98**, 253001 (2007).
- 551 [13] P. Ranitovic, X. M. Tong, C. W. Hogle, X. Zhou, Y. Liu, N. Toshima, M. M. Murnane, and  
552 H. C. Kapteyn, Phys. Rev. Lett. **106**, 193008 (2011).
- 553 [14] X. M. Tong and N. Toshima, Phys. Rev. A **81**, 063403 (2010).
- 554 [15] L. B. Madsen, P. Schlagheck, and P. Lambropoulos, Phys. Rev. A **62**, 062719 (2000).
- 555 [16] M. Domke, K. Schulz, G. Remmers, G. Kaindl, and D. Wintgen,  
556 Phys. Rev. A **53**, 1424 (1996).
- 557 [17] A. Bürgers, D. Wintgen, and J. M. Rost, J. Phys. B: At., Mol. Opt. Phys. **28**, 3163 (1995).
- 558 [18] M. Aymar, C. H. Greene, and E. Luc-Koenig, Rev. Mod. Phys. **68**, 1015 (1996).
- 559 [19] G. Lagmago Kamta and A. F. Starace, Phys. Rev. A **65**, 053418 (2002).
- 560 [20] U. V. Riss and H. D. Meyer, J. Phys. B: At. Mol. Opt. Phys. **26**, 4503 (1993).
- 561 [21] H. Bachau, E. Cormier, P. Decleva, J. E. Hansen, and F. Martín, Rep. Prog. Phys. **64**, 1815  
562 (2001).
- 563 [22] C. W. McCurdy, D. A. Horner, T. N. Rescigno, and F. Martín,  
564 Phys. Rev. A **69**, 032707 (2004).
- 565 [23] A. Palacios, T. N. Rescigno, and C. W. McCurdy, Phys. Rev. A **77**, 032716 (2008).
- 566 [24] N. Moiseyev, Phys. Rep. **302**, 212 (1998).
- 567 [25] I. I. Sobelman, *Introduction to the theory of atomic spectra* (Pergamon Press Oxford, New  
568 York, 1972).
- 569 [26] A. Becker and F. H. M. Faisal, Phys. Rev. A **59**, R1742 (1999).
- 570 [27] T. Nubbemeyer, K. Gorling, A. Saenz, U. Eichmann, and W. Sandner,  
571 Phys. Rev. Lett. **101**, 233001 (2008).
- 572 [28] M. Awasthi, Y. V. Vanne, and A. Saenz, J. Phys. B: At. Mol. Opt. Phys. **38**, 3973 (2005).
- 573 [29] J. Bayfield, *Quantum evolution: an introduction to time-dependent quantum mechanics*  
574 (John Wiley, 1999).
- 575 [30] A. Palacios, C. W. McCurdy, and T. N. Rescigno, Phys. Rev. A **76**, 043420 (2007).
- 576 [31] S. Bashkin and J. J.O. Stoner, *Atomic Energy Levels and Grotrian Diagrams – vol. I. Hydrogen*  
577 *I – Phosphorus XV* (North Holland Publ. Co., Amsterdam, 1975).